Runtime Composition of Iterations for Fusing Loop-carried Sparse Dependence

Kazem Cheshmi*
McMaster University
Hamilton, Canada
cheshmi@mcmaster.ca

Michelle Mills Strout
University of Arizona and HPE
Tucson, USA
mstrout@cs.arizona.edu

Maryam Mehri Dehnavi
University of Toronto
Toronto, Canada
mmehride@cs.toronto.edu

ABSTRACT

Dependence between iterations in sparse computations causes inefficient use of memory and computation resources. This paper proposes sparse fusion, a technique that generates efficient parallel code for the combination of two sparse matrix kernels, where at least one of the kernels has loop-carried dependencies. Existing implementations optimize individual sparse kernels separately. However, this approach leads to synchronization overheads and load imbalance due to the irregular dependence patterns of sparse kernels, as well as inefficient cache usage due to their irregular memory access patterns. Sparse fusion uses a novel inspection strategy and code transformation to generate parallel fused code optimized for data locality and load balance. Sparse fusion outperforms the best of unfused implementations using ParSy and MKL by an average of 4.2× and is faster than the best of fused implementations using existing scheduling algorithms, such as LBC, DAGP, and wavefront by an average of 4× for various kernel combinations.

CCS CONCEPTS

• **Software and its engineering** → *Runtime environments.*

ACM Reference Format:
Kazem Cheshmi, Michelle Mills Strout, and Maryam Mehri Dehnavi. 2023. Runtime Composition of Iterations for Fusing Loop-carried Sparse Dependence . In *The International Conference for High Performance Computing, Networking, Storage and Analysis (SC '23), November 12–17, 2023, Denver, CO, USA.* ACM, New York, NY, USA, 13 pages. https://doi.org/10.1145/3581784.3607097

*The work is mainly done while the author was at the University of Toronto.

SC '23, November 12–17, 2023, Denver, CO, USA

ACM ISBN 979-8-4007-0109-2/23/11…$15.00
https://doi.org/10.1145/3581784.3607097

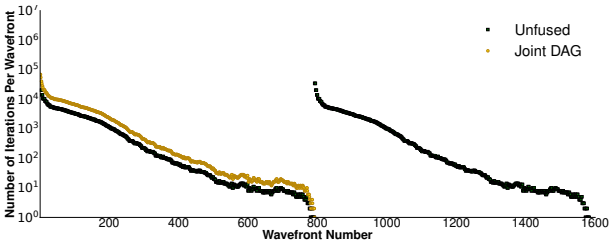

Figure 1: The nonuniform parallelism in the DAGs of sparse incomplete Cholesky and triangular solver (annotated with unfused) and for the joint DAG of the two kernels results in load imbalance. Higher value in the y-axis shows high parallelism in a given wavefront. Wavefront numbers in the x-axis are numbered based on their order of execution.

1 INTRODUCTION

Numerical algorithms [32] and optimization methods [5, 11, 36] often involve numerous consecutive sparse matrix computations. For example, in iterative solvers [32] such as Krylov methods [13, 33], sparse kernels that apply a preconditioner are repeatedly executed inside and between iterations of the solver. Sparse kernels with loop-carried dependencies, i.e., kernels with partial parallelism, are frequently used in numerical algorithms, and the performance of scientific simulations relies heavily on efficient parallel implementations of these computations. Sparse kernels that exhibit partial parallelism often have multiple wavefronts of parallel computation where a synchronization is required for each wavefront, i.e., wavefront parallelism [19, 44]. The amount of parallelism varies per wavefront and often tapers off toward the end of the computation, which results in load imbalance. Figure 1 shows with dark lines the nonuniform parallelism for the sparse incomplete Cholesky (SpIC0) and the sparse triangular solve (SpTRSV) kernels when SpTRSV executes after SpIC0 completes. Separately optimizing such kernels exacerbates this problem by adding even more synchronization. Also, opportunities for data reuse between two sparse computations might not be realized when sparse kernels are optimized separately.

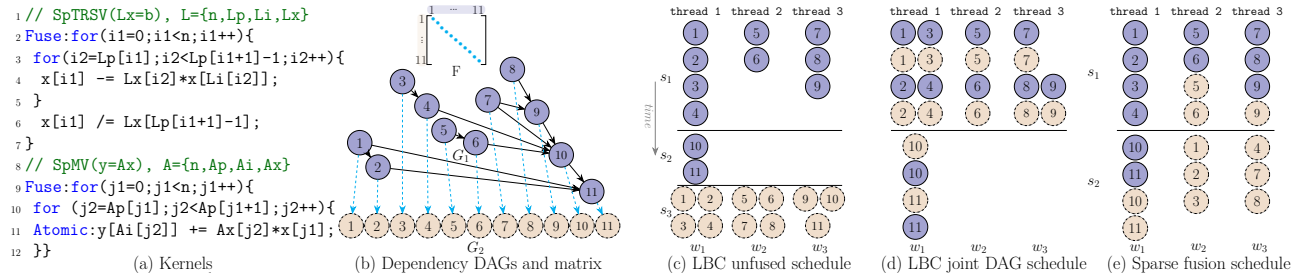

(a) Kernels (b) Dependency DAGs and matrix (c) LBC unfused schedule (d) LBC joint DAG schedule (e) Sparse fusion schedule

Figure 2: Solid purple (G_1) and dash-dotted yellow (G_2) vertices in Figure 2b represent the iterations of SpTRSV and SpMV kernels shown in Figure 2a, respectively, and edges show the dependencies between iterations. Figures 2c-2e show three different schedules for running SpTRSV followed by SpMV as shown in Figure 2b, where the number of processors (r) is three. Dashed edges in Figure 2b show the dependencies between the two kernels and correspond to the nonzero elements of matrix F. The unfused implementation schedules each DAG separately, as shown in Figure 2c. Two different fused implementations in Figures 2d and 2e use both DAGs and the dependencies between kernels to build a fused schedule.

Instead of iterations of sparse kernels being scheduled separately, they can be scheduled jointly. Wavefront parallelism can be applied to the joint DAG of two sparse computations. A data flow directed acyclic graph (DAG) describes the dependencies between iterations of a kernel [9, 22, 40]. A joint DAG includes all of the dependencies between iterations within and across kernels. The joint DAG of sparse kernels with partial parallelism and the DAG of another sparse kernel provides slightly more parallelism per wavefront without increasing the number of wavefronts. The yellow line in Figure 1 shows how scheduling the joint DAG of SpIC0 and SpTRSV increases the parallelism per wavefront and significantly reduces the number of wavefronts (synchronizations). However, the load balance issues remain, and there are still several synchronizations.

Wavefronts of the joint DAG can be aggregated to reduce the number of synchronizations. However, existing DAG partitioners such as Load-Balanced Level Coarsening (LBC) [10] and DAGP [23] may not achieve good load balance when applied to the joint DAG, because they aggregate iterations from consecutive wavefronts, which may have different amounts of parallelism. Moreover, by aggregating iterations from wavefronts in the joint DAG, DAG partitioning methods may improve the temporal locality between the two kernels, but this can compromise the spatial locality within each kernel. For example, for two sparse kernels that only share a small array and operate on different sparse matrices, optimizing temporal locality between kernels will not be beneficial. Finally, due to the dependence between kernels, the number of dependence edges per iteration increases, e.g., between 0.2–40% for matrices in this study, making it challenging for existing DAG partitioners to create balanced workloads for all cores.

We present sparse fusion, a technique that creates an efficient schedule and fused code for combining a sparse kernel with loop-carried dependencies and another sparse kernel. Sparse fusion uses an inspector to apply a novel iteration composition and ordering (ICO) runtime scheduling algorithm on the DAGs of the two input sparse kernels. ICO uses a vertex dispersion strategy to balance the workloads in the fused schedule, uses two novel iteration packing heuristics to improve the data locality by exploiting the spatial and temporal locality of the merged computations, and uses vertex pairing strategies to aggregate iterations without explicitly joining the DAGs.

Motivation Example. Figure 2 compares the schedule created by sparse fusion (sparse fusion schedule) with the schedules created by applying LBC to the individual DAGs of each sparse kernel (LBC unfused schedule) and LBC applied to the joint DAG (LBC joint DAG schedule). All approaches take the input DAGs in Figure 2b. Solid purple vertices represent the DAG of sparse triangular solve (SpTRSV), and the dash-dotted yellow vertices correspond to sparse matrix-vector multiplication (SpMV). LBC is a DAG partitioner that partitions a DAG into a set of aggregated wavefronts called s-partitions that run sequentially, each s-partition is composed of some independent w-partitions. In the LBC unfused schedule in Figure 2c, LBC partitions the SpTRSV DAG and creates two s-partitions, i.e., s_1 and s_2. The vertices of SpMV are scheduled to run in parallel in a separate wavefront s_3. This implementation is not load-balanced since the number of partitions that can run in parallel differs for each s-partition. In the LBC joint DAG schedule, the DAGs are first joined using the dependency information between the two kernels shown with blue dotted arrows, and then LBC is applied to create the two s-partitions in Figure 2d. These s-partitions

are also not load balanced, for example, s_2 only has one partition. Throughout the paper, load balance for s-partitions means that each s-partition needs to have balanced workloads among its own computations. Sparse fusion uses ICO to first partition the SpTRSV DAG and then disperses the SpMV iterations to create load-balanced s-partitions, e.g., the two s-partitions in Figure 2e have three closely balanced partitions.

SpTRSV solves $Lx = b$ to find x, and SpMV performs $y = A * x$ where L is a sparse lower triangular matrix, A is a sparse matrix, and x, b, and y are vectors. The LBC joint DAG schedule interleaves iterations of the two kernels to reuse x. However, this can compromise spatial locality within each kernel because the shared data between the two kernels, x, is smaller than the amount of data used within each kernel, A and L. With the help of a reuse metric, sparse fusion realizes the larger data accesses inside each kernel and hence packs iterations to improve spatial locality within each kernel.

We implement sparse fusion as an embedded domain-specific library in C++ that takes the specifications of the sparse kernels as input and generates an efficient and correct parallel fused code. The primary focus of sparse fusion is to fuse two sparse kernels where at least one of the kernels has a loop-carried dependence. We test sparse fusion on six of the most commonly used sparse kernel combinations in scientific codes, which include kernels such as SpTRSV, SpMV, incomplete Cholesky, incomplete LU, and diagonal scaling. We evaluate sparse fusion against unfused and fused implementations across all symmetric positive definite matrices larger than 100K nonzero elements from SuiteSparse [15]. Sparse fusion is faster than the best of unfused implementations using MKL or ParSy by an average factor of 4.2× and is faster than the best-fused implementations using LBC, DAGP, and wavefront techniques applied to the joint DAG by an average factor of 4×. We also use sparse fusion to fuse more than two loops in the Gauss-Seidel kernel, resulting in an average speedup of 1.3× and 1.8× compared to ParSy and the best of Joint-DAG respectively.

2 SPARSE FUSION

Sparse fusion is implemented as an inspector-executor technique that can be used as a library. The inspector includes the ICO algorithm and functions that generate its inputs, i.e. dependency DAGs, reuse ratio, and the dependency matrix. The executor is the fused code that is created by the fused transformation.

2.1 Overview

For every kernel pair, sparse fusion generates an inspector and an executor, such as Listing 1, for the kernels in Figure 2a. The inspector first builds the inputs to ICO using

```
1  #include "TrsvMv.h"
2  #include "ICO.h"
3  void main(){
4   L.load();A.load();b.load();
5  /// -------- Inspector -------- ///
6   G1 = SpTRSV.intra_DAG(L);//Sec 2.2
7   G2 = SpMV.intra_DAG(A);
8   F = inter_DAG(A,L,b,x,y);//Sec 2.2
9   reuse_ratio = compute_reuse(A,L,b,x,y); //Sec 2.2
10  FusedSchedule = ICO(G1,G2,F,r,reuse_ratio); //Sec 3
11 /// -------- Executor -------- ///
12  fused_code(L,b,A,x,y,FusedSchedule,reuse_ratio); //Sec 2.3
13 }
```

Listing 1: Sparse fusion's driver code.

the functions intra_DAG, inter_DAG, and compute_reuse in lines 6–8 in Listing 1 and then calls ICO in line 10 to generate FusedSchedule for r threads. Then the executor code, fused_code in line 12 in Listing 1, runs in parallel using the fused schedule. The fused schedule can be reused as long as the sparsity patterns of A and L do not change.

2.2 The Inspector in Sparse Fusion

The inputs of the ICO algorithm are the dependency matrix between kernels, the DAG of each kernel, and a reuse ratio. Sparse fusion analyzes the kernel code to generate inspector components that create these inputs.

Dependency DAGs: Lines 6–7 in Figure 1 use an internal domain-specific library to generate the dependency DAG of each kernel. General approaches such as the work by Mohammadi et al. [31] can also be used to generate the DAGs, however, that would lead to higher inspection times compared to a domain-specific approach. For example, with domain knowledge, sparse fusion will use the L matrix as the SpTRSV DAG G_1 in Figure 2b. Each nonzero L_{ij} represents a dependency from iteration i to j.

```
Matrix inter_DAG(CSR A,CSC L,double *b,double *x,double *y){
 for(i1=0; i1<A.n; i1++){
  j1 = i1;
  if(A.p[j1] < A.p[j1+1] )
   F[j1].append(i1); }
  return F;}
```

Listing 2: inter_DAG function for the example in Figure 2a.

Dependency Matrix F: ICO uses the dependency information between kernels to create a correct fused schedule. By running the inter_DAG function, sparse fusion creates this information and stores it in matrix F. To generate inter_DAG, sparse fusion finds dependencies between statements of the two kernels by analyzing the body of the outermost loop of kernels. Each nonzero $F_{i,j}$ represents a dependency from

```
1 Fuse:for(I1){//loop 1
2  ...
3   for(In)
4    x[h(I1,...,In)] = a*y[g(I1,...,In)];
5  }
6 Fuse:for(J1){//loop 2
7 ...
8   for(Jm)
9    z[h'(J1,...,Jm)] = a*x[g'(J1,...,Jm)];
10 }
```

(a) Before

```
1 if(FusedSchedule.fusion && reuse_ratio < 1){
2  for (every s-partition s){
3 #pragma omp parallel for
4   for (every w-partition w){
5    for(v ∈ FusedSchedule[s][w].L1){//loop 1
6     ...
7     for(In)
8       x[h(v,...,In)] = a*y[g(v,...,In)];
9    }
10   for(v ∈ FusedSchedule[s][w].L2){//loop 2
11    ...
12    for(Jm)
13      z[h'(v,...,Jm)] = a*x[g'(v,...,Jm)];
14  }}}}
```

(b) After - separated variant

```
1 if(FusedSchedule.fusion && reuse_ratio >= 1){
2  for (every s-partition s){
3 #pragma omp parallel for
4   for (every w-partition w){
5    for(v ∈ FusedSchedule[s][w]){
6     if(v.type == L1){//loop 1
7      for(In)
8       x[h(v.id,...,In)] = a*y[g(v,...,In)];
9
10    } else {//loop 2
11     for(Jm)
12      z[h'(v.id,...,Jm)] = a*x[g'(v,...,Jm)];
13    }
14  }}}}
```

(c) After - interleaved variant

Figure 3: The general form of the sparse fusion code transformation with its two variants, interleaved and separated. `I1...In` and `J1...Jm` represent two loop nests. `h'` and `g'` are data access functions. `FusedSchedule` contains the schedule for iterations of loops `I1`, shown with `L1` and `J1`, shown with `L2`.

iteration j of the first loop, i.e., column j of F, to iteration i of the second loop, i.e., row i of F. In Figure 2a, there exists a read after write (flow) dependency between statements `x[i1]` in line 6 and `x[j1]` in line 11. As a result, sparse fusion generates the function shown in Listing 2. The resulting F matrix, generated at runtime, is shown in Figure 2b.

Reuse Ratio: ICO uses a reuse ratio based on the memory access patterns of the kernels to decide whether to improve locality within kernels or between them. The inspector in line 9 in Listing 1 computes the reuse ratio metric. The metric represents the ratio of common to total memory accesses of the two kernels, i.e., $\frac{2*\text{common memory access}}{\max(\text{kernel1 accesses, kernel2 accesses})}$. For a reuse ratio larger than one, the number of common accesses between the two kernels is larger than the accesses inside a kernel. Sparse fusion estimates memory accesses using the ratio of the size of common variables over the maximum of the total size of variables among the kernels. For the running example, the code generated for `compute_reuse` is `2*x.n / max(A.size+x.n+y.n,L.size+x.n+b.n)`. Since `x` is smaller than $L.size$ or $A.size$, the reuse ratio is less than one.

2.3 Fused Code

To generate the fused code, a fused transformation is applied to the two loops at compile-time, and two variants of the fused code are generated, shown in Figure 3. The transformation variants are *separated* and *interleaved*. The fused code uses the reuse ratio at runtime to select the appropriate variant for the specific input. Figure 3a shows the input sequential loops, which are annotated with `Fuse`, and are transformed to the separated and interleaved code variants as shown in Figures 3b and 3c, respectively. The separated variant is selected when the reuse ratio is smaller than one. In this variant, iterations of one of the loops run consecutively without checking the loop type. The interleaved variant is chosen when the reuse ratio is larger than one. In this variant, iterations of both loops run interleaved, and the variant checks the loop type for each iteration, as shown in lines 6 and 10 in Figure 3c.

3 ITERATION COMPOSITION AND ORDERING

Sparse fusion uses the iteration composition and ordering (ICO) algorithm to create an efficient fused partitioning that will be used to schedule iterations of the fused code. ICO partitions vertices of the DAGs of the two input loops to create parallel load-balanced workloads for all cores while improving locality within each thread. This section describes the inputs, output, and three steps of the ICO algorithm (Algorithm 1) using the running example in Figures 2 and 4.

3.1 Inputs and Output to ICO

The inputs to ICO (shown in Algorithm 1) are two DAGs G_1 and G_2 from the lexicographically first and second input loops, respectively, and the inter-DAG dependency matrix F that stores the dependencies between loops. A DAG shown with $G_j(V_j, E_j, c)$ has a vertex set V_j and an edge set E_j and a non-negative integer weight $c(v_i)$ for each vertex $v_i \in V_j$. The vertex v_i of G_j represents iteration i of a loop, and each edge shows a dependency between two loop iterations. Therefore, we use vertex and iteration interchangeably and similarly DAG and loop. $c(v_i)$ is the computational load of a loop and is defined as the total number of nonzeros touched to complete its computation. Other inputs to the algorithm are the number of requested partitions r, which is set to the number of cores, and the reuse ratio discussed in section 2.2.

The output of ICO is a *fused partitioning* $\mathcal{V}$ that has $b \geq 1$ s-partitions, each s-partition contains up to $k > 1$ w-partitions, where $k \leq r$. ICO creates b disjoint s-partitions from vertices of both DAGs, shown with $\mathcal{V}s_i$ where $\cup i = 0^b \mathcal{V}s_i = V_1 \cup V_2$. Each s-partition includes vertices from a lower bound and upper bound of wavefront numbers shown with $s_i = [lb_i..ub_i)$ as well as some *slack vertices*. For each s-partition $\mathcal{V}s_i$, ICO creates $m_i \leq k$ independent *w-partitions* $\mathcal{V}s_i, w_j$

where $\mathcal{V}s_i, w_1 \cup ... \cup \mathcal{V}s_i, wm_i = \mathcal{V}_{s_i}$. Since w-partitions are independent, they can run in parallel.

Example. In Figure 2b, the SpTRSV DAG G_1, the SpMV DAG G_2, and the inter-DAG dependency matrix F are inputs to ICO. Other inputs to ICO are r=3 and the $reuse_ratio$. The fused partitioning shown in Figure 2e has two s-partitions (b=2). The first s-partition has three w-partitions (m_1=3) shown with $\mathcal{V}_{s_1}$ = [1, 2, 3, 4]; [5, 6, 5, 6]; [7, 8, 9, 9], where the underscored vertices belong to G_1.

3.2 The ICO Algorithm

Algorithm 1 shows the ICO algorithm. It takes the inputs and goes through three steps of *(1)* vertex partitioning and partition pairing with the objective to compose iterations of two loops that can run independently; *(2)* merging and slack vertex assignment to reduce synchronization and to balance workloads; and *(3)* packing to improve thread locality.

3.2.1 Vertex Partitioning and Partition Pairing. The first step of ICO partitions one of the input DAGs G_1 or G_2, and then uses that partitioning to partition the other DAG. The created partitions are stored in $\mathcal{V}$. Due to inter-DAG dependence, the number of dependent edges between iterations increases after fusion, posing challenges to load balancing. For example, across the studied kernels in this paper and for all symmetric positive definite (SPD) matrices with nonzeros larger than 100K in SuiteSparse [15], the average number of edges per vertex increases between 0.2–40% after fusion. To find independent workloads for threads, ICO ignores the dependencies across loops and first creates a partitioning from one of the DAGs with the help of *vertex partitioning*. Then the other DAG is partitioned using a *partition pairing* strategy. The DAG that is partitioned first is the head DAG and the other is the tail DAG. The joint-DAG does need to be explicitly created in this two-step process, enabling scalability.

Vertex partitioning. ICO first selects the DAG with edges as the head DAG in line 1 in Algorithm 1. Then it uses the LBC DAG partitioner [10] to construct a partitioning of the head DAG, G_h, in line 2 of Algorithm 1 by calling the function `LBC`. The resulting partitioning has a set of disjoint s-partitions. Each s-partition contains k disjoint w-partitions which are balanced using vertex weights. Disjoint w-partitions ensure all w-partitions within s-partitions are independent. The created partitions are stored in a two-dimensional list H using `list`.

Partition pairing. The algorithm then partitions the tail DAG using partition pairing. Pair-partitions are *self-contained* so that they can execute in parallel if assigned to the same s-partition. The created partitions are put in the fused partitioning $\mathcal{V}$ to be used in step two. Pair partitions H_{ij} and T_{ij} are called self-contained if all reachable vertices from a

Algorithm 1: The ICO algorithm.

```
   Input  : G1(V1, E1, c1), G2(V2, E2, c2), F, r, reuse_ratio
   Output : V
   /* (i) Vertex partitioning and partition pairing     */
1  if E2 > 0 then Gh = G2 else Gh = G1;
2  [H, k] = LBC(Gh, r).list(), T = ∅, V = ∅
3  for (every partition Hi,j) do          // Partition pairing
4  |  Ti,j = BFS(Hi,j, F, Gh)
5  |  Ui,j = Ti,j.remove_uncontained(F)
6  |  Gp.add(Hi,j, Ti,j, Ui,j)
7  end
   /* (ii) Merging and slacked vertex assignment        */
8  S = slack_info(Gp)
9  for (every w-partition pair (w, w') ∈ Gp.pairs) do
10 |  if (SN(w) = 0) ∧ (SN(w') = 0) then Gp.merge(w,w')
11 end
12 V = Gp − S, ϵ = |V| × 0.001
13 for (every s-partition Vsi ∈ V) do
14 |  S = Vsi.balance_with_slack(S, ϵ)
15 |  if S ≠ ∅ then S = Vsi.assign_even(S)
16 end
   /* (iii) Packing                                     */
17 if reuse_ratio ≥ 1 then V.interleaved_pack(F)
18 else V.separated_pack()
```

breadth-first search (BFS) on $\forall v \in H_{ij} \cup T_{ij}$ through vertices of G_1 and G_2 are in $H_{ij} \cup T_{ij}$. Self-contained pair partitions (H_{ip}, T_{ip}) and (H_{iq}, T_{iq}) can execute in parallel without synchronization if they are in the same wavefront i. Partitions that do not satisfy this condition create synchronization in the final schedule.

Lines 3–7 show the partitioning of the tail DAG by performing a BFS on the dependence matrix, starting from the head DAG partitioning H. Then in line 5, partition pairing removes vertices whose dependence is not satisfied by calling the `remove_uncontained` function. This step ensures the self-contained condition. Finally, in line 6, the created partitions are added to the partitioned graph P_G where each vertex of P_G is a partition and edges represent dependence.

Example. Figure 4b shows the output of ICO after the first step for the inputs in Figure 2b. ICO chooses G_1 as the head DAG because it has edges ($|E_1| > 0$), while G_2 has no edges. In vertex partitioning, G_1 is partitioned with LBC to create up to three w-partitions (because $r = 3$) per s-partition. The created partitions are shown in Figure 4a and are stored in H. The first s-partition $\mathcal{V}s_1$ is stored in H_1. The three w-partitions of $\mathcal{V}s_1$ are indexed with $H_{1,1}$, $H_{1,2}$, and $H_{1,3}$. Similarly, $\mathcal{V}_{s_2}$ is stored in H_2. Figure 4b shows the partitioned graph G_p after partition pairing.

3.2.2 Merging and Slack Vertex Assignment. The second step of ICO reduces the number of synchronizations by merging

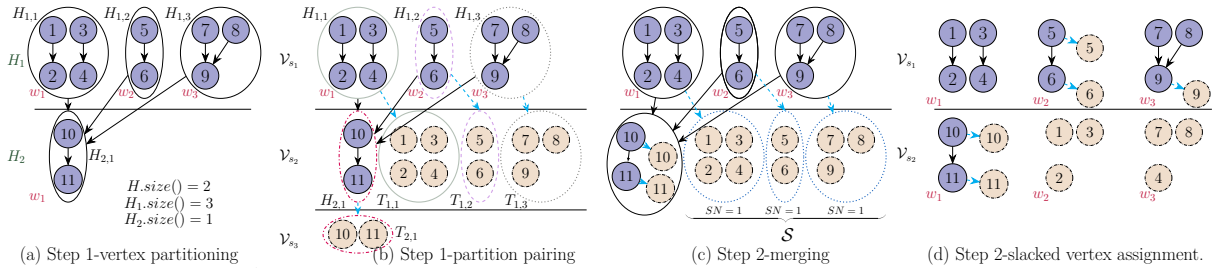

(a) Step 1-vertex partitioning (b) Step 1-partition pairing (c) Step 2-merging (d) Step 2-slacked vertex assignment.

Figure 4: Stages of ICO for DAGs G_1 and G_2 and matrix F in the running example shown in Figure 2b where the reuse ratio ($reuse\_ratio$) is smaller than one and number of processors (r) is three. The first step of the algorithm selects G_1 and creates H partitioning for three processors as shown in Figure 4a. Then it pairs each $H_{i,j}$ through dependencies in matrix F to create partitioning T of G_2 as shown in Figure 4b. The partitions with the same line pattern/color are pair partitions. In the second step, ICO merges pair partitions that cannot be dispersed such as first w-partitions of s-partitions 2 and 3 ($\mathcal{V}_{s_3,w_1}$ and $\mathcal{V}_{s_2,w_1}$) in Figure 4b. Slack vertices, $\mathcal{S}$, are shown with blue dotted circles in Figure 4c. Slack vertices are assigned into imbalanced w-partitions as shown in Figure 4d. Since the reuse ratio is smaller than one, vertices inside each partition are packed separately as shown in Figure 2e.

some of the pair partitions in a *merging* phase. It also improves load balance by dispersing vertices across partitions using *slack vertex assignment*.

Slack definitions. A vertex v can always run in its wavefront number $l(v)$. However, the execution of vertex v can sometimes be postponed up to $SN(v)$ wavefronts without the need to move its dependent vertices to later wavefronts. $SN(v)$ is the slack number of v and is defined as $SN(v) = P_G - l(v) - height(v)$ where $height(v)$ is the maximum path from a vertex v to a sink vertex (a sink vertex is a vertex with no outgoing edge), P_G is the critical path of G, and $l(v)$ is the wavefront number of v. A vertex with a positive slack number is a *slack vertex*. To compute vertex slack numbers efficiently, instead of visiting all vertices, ICO iterates over partitions (G_p) and computes the slack number of each partition in the partitioned DAG, i.e., *partition slack number*. The computed slack number for a partition is assigned to all vertices of the partition. As shown in line 8 of Algorithm 1, all partition slack numbers of G_p are computed via `slack_info` and are stored in $\mathcal{S}$. For example, since vertices in $\mathcal{V}s_2, w_3$ can be postponed one wavefront, from s-partition 2 to 3, their slack number is 1. Vertices in w-partitions $\mathcal{V}s_2, w_1$ and $\mathcal{V}_{s_3,w_1}$ cannot be moved because their slack numbers are zero.

Merging. ICO finds pair partitions with partition slack number of zero and then merges them as shown in lines 9-11. Since pair partitions are self-contained, merging them does not affect the correctness of the schedule. Algorithm 1 visits all pair partitions (w, w') in $G_p.pairs$ and merges them using the `merge` function in line 10 if their slack numbers are zero, i.e., $SN(w) = 0$ and $SN(w') = 0$.

Slacked vertex assignment. The algorithm then reorders slacked vertices to approximately load balance the w-partitions of an s-partition using a cost model. The cost of w-partition $w \in \mathcal{V}s_i$ is defined as $cost(w) = \sum v \in wc(v)$. A w-partition is balanced if its maximal difference is smaller than a threshold ϵ. The maximal difference for a w-partition inside an s-partition is computed by subtracting its cost from the cost of the w-partition (from the same s-partition) with the maximum cost. ICO first removes all slacked vertices $\mathcal{S}$ from the G_p and stores it as fused partitioning $\mathcal{V}$ in line 12. It then goes over every s-partition i and balances $\mathcal{V}s_i$ by assigning a slacked vertex to its imbalanced w-partition. The function `balance_with_slack` in line 14 balances each partition using either a slack vertex of the pair partition or a slack vertex $v_l \in \mathcal{S}$ from any other partition that satisfies $l(v_l) < i < (l(v_l) + SN(v_l))$. In line 15, slacked vertices in $\mathcal{S}$ that are not postponed to later s-partitions are evenly divided between the w-partitions of the current s-partition ($\mathcal{V}s_i$) using the `assign_even` function.

Example. Figure 4d shows the output of the second step of ICO from the partitioning in Figure 4b. First, pair partitions $(\mathcal{V}s_2, w_1, \mathcal{V}s_3, w_1)$, shown with red dash-dotted circles in Figure 4b, are merged because their slack numbers are zero. The resulting merged partition is shown in Figure 4c. Then slacked vertex assignment balances the w-partitions in Figure 4c. The balanced partitions are shown in Figure 4d. The slacked vertices, S, are shown with dotted blue circles in Figure 4c. The w-partitions in $\mathcal{V}s_1$ are balanced using vertices of their pair partitions, e.g., the yellow dash-dotted vertices 5 and 6 are moved to w_2 in $\mathcal{V}s_1$ as shown in Figure 4d. The second strategy in `balance_with_slack` is used to balance partitions in $\mathcal{V}s_2$. This is because the slack vertices in S can execute in either s-partition two or three, since they are from s-partition one and have a slack number of one, and they are used to balance the w-partitions in $\mathcal{V}s_2$.

3.2.3 Packing. The third step of ICO reorders the vertices inside a w-partition to improve data locality for a thread. The previous steps of the algorithm create w-partitions that are composed of vertices of one or both kernels, but the order of execution is not defined. Using the reuse ratio, the order in which the nodes in a w-partition should be executed is determined with a packing strategy. ICO has two packing strategies: *(i)* in interleaved packing, the iterations of the two loops are interleaved to improve temporal locality between loops and *(ii)* in separated packing, the vertices of each kernel are executed separately to benefit from spatial locality within iterations of a loop. When the reuse ratio is greater than one, in line 17 of Algorithm 1, the function `interleaved_pack` is called to interleave iterations of the two kernels based on F. Otherwise, `separated_pack` is called in line 18.

Example. Figure 2e shows the output of ICO's third step from the partitioning in Figure 4d. Since the reuse ratio is smaller than one, separated packing is chosen and $\mathcal{V}s_2, w_1$ is stored as $\mathcal{V}s_2, w_1 = [\underline{10}, \underline{11}, 10, 11]$. Vertices are ordered to keep dependent iterations of SpTRSV and consecutive iterations of SpMV next to each other.

3.3 Fusing More than Two Loops

The ICO algorithm processes one loop at a time and thus efficiently supports the fusion of any number of loops without the explicit creation of the joint DAG, which can be infeasible. For more than two loops, ICO processes their DAGs in the order they appear in the code. The first two loops are fused as described in Section 3.2. Partition pairing uses the final partitioned fused schedule of the previous loop as the new head and the additional DAG as a tail. In the second step, ICO finds slacked partitions and applies merging and slack vertex assignment as described in Section 3.2.2. And finally, vertices inside each w-partition are sorted based on ICO packing strategies. It is important to note that sparse fusion always applies fusion. When fusing loops is not profitable, sparse fusion performance becomes almost identical to the unfused performance. We will discuss the efficiency of ICO for more than one loop using a case study in the experimental results section.

4 EXPERIMENTAL RESULTS

We compare the performance of sparse fusion to MKL [46] and ParSy [10], two state-of-the-art tools that accelerate individual sparse kernels, which we call unfused implementations. Sparse fusion is also compared to the three fused implementations that we create. To our knowledge, sparse fusion is the first work that provides a fused implementation of sparse kernels where at least one kernel has loop-carried dependencies. For comparison, we also create three fused implementations of sparse kernels by applying LBC, DAGP, and a wavefront technique to the joint DAG of the two input sparse kernels and creating a schedule for execution using the created partitioning. The methods will be referred to as fused LBC, fused DAGP, and fused wavefront, respectively.

4.1 Setup.

All symmetric positive definite matrices larger than 100K nonzeros from [15] are used for experimental results. The matrix values are real and stored in double precision. The test-bed architecture is a multicore processor with 20 Intel CascadeLake cores at 2.5 GHz with 33 MB L3 Cache. All generated codes, implementations of different approaches, and library drivers are compiled with GCC v.11.3.0 compiler and with the `-O3` flag. Each thread is pinned to a physical core and a close thread binding is selected. Matrices are first reordered with METIS [25] to improve thread parallelism.

We compare sparse fusion with two unfused implementations where each kernel is optimized separately: *I. ParSy* applies LBC to DAGs that have edges. For parallel loops, the method runs all iterations in parallel. LBC is developed for L-factors [14] or chordal DAGs. Thus, we make DAGs chordal before using LBC. *II. MKL* uses Intel MKL [46] routines with MKL 2021.1.0 and calls them separately for each kernel. We use the inspector executor version of MKL by calling `mkl_sparse_set_sv_hint`, `mkl_sparse_set_mv_hint`, and `mkl_sparse_optimize` for inspection. For the executor of SpTRSV, SpMV, and SpILU0 we use `mkl_sparse_d_trsv`, `mkl_sparse_d_mv`, and `dcsrilu0`, respectively.

Sparse fusion is also compared to three fused approaches, all of which take as input the *joint DAG*; the joint DAG is created by combining the DAGs of the input kernels using the inter-DAG dependency matrix F. We then implement three approaches to build the fused schedule from the joint DAG: *I. Fused wavefront* traverses the joint DAG in topological order and builds a list of wavefronts that show vertices of both DAGs that can run in parallel. *II. Fused LBC* applies the LBC algorithm to the joint DAG and creates a set of s-partitions, each composed of independent w-partitions. LBC is taken from ParSy and its parameters are tuned for best performance. We use 4 for `initial_cut` and 400 for `coarsening_factor`. *III. Fused DAGP* applies the DAGP partitioning algorithm to the joint DAG and then executes all independent partitions that are in the same wavefront in parallel. DAGP is used with METIS for its initial partitioning, with one run (`runs=1`), and the remaining parameters are set to default. All fused approaches use sparse fusion packing.

The list of sparse kernel combinations investigated is in Table 1. To demonstrate sparse fusion's capabilities, the sparse kernels are selected with different combinations of storage formats, i.e., CSR and compressed sparse column (CSC) storage, different combinations of parallel loops and loops with

Table 1: The list of kernel combinations. CD: loops with carried dependencies, SpIC0: Sparse Incomplete Cholesky with zero fill-in, SpILU0: Sparse Incomplete LU with zero fill-in, DSCAL: scaling rows and columns of a sparse matrix.

ID	Kernel combination	Operations	Dependency DAGs	Reuse Ratio
1	SpTRSV CSR - SpTRSV CSR	$x = L^{-1}y, z = L^{-1}x$	CD - CD	$\frac{2n+2size_L}{max(2n+size_L,size_L+2n)} \geq 1$
2	DSCAL CSR - SpILU0 CSR	$LU \approx DAD^T$	Parallel - CD	$\frac{2size_A}{max(size_A,size_A+2n)} \geq 1$
3	SpTRSV CSR - SpMV CSC	$y = L^{-1}x, z = Ay$	CD - Parallel	$\frac{2n}{max(2n+size_L,size_A+2n)} < 1$
4	SpIC0 CSC - SpTRSV CSC	$LL^T \approx A, y = L^{-1}x$	CD - CD	$\frac{2size_L}{max(size_L,size_L+2n)} \geq 1$
5	SpILU0 CSR - SpTRSV CSR	$LU \approx A, y = L^{-1}x$	CD - CD	$\frac{2size_A}{max(size_A,size_L+2n)} \geq 1$
6	DSCAL CSC - SpIC0 CSC	$LL^T \approx DAD^T$	Parallel - CD	$\frac{2size_L}{max(size_L,size_L+2n)} \geq 1$

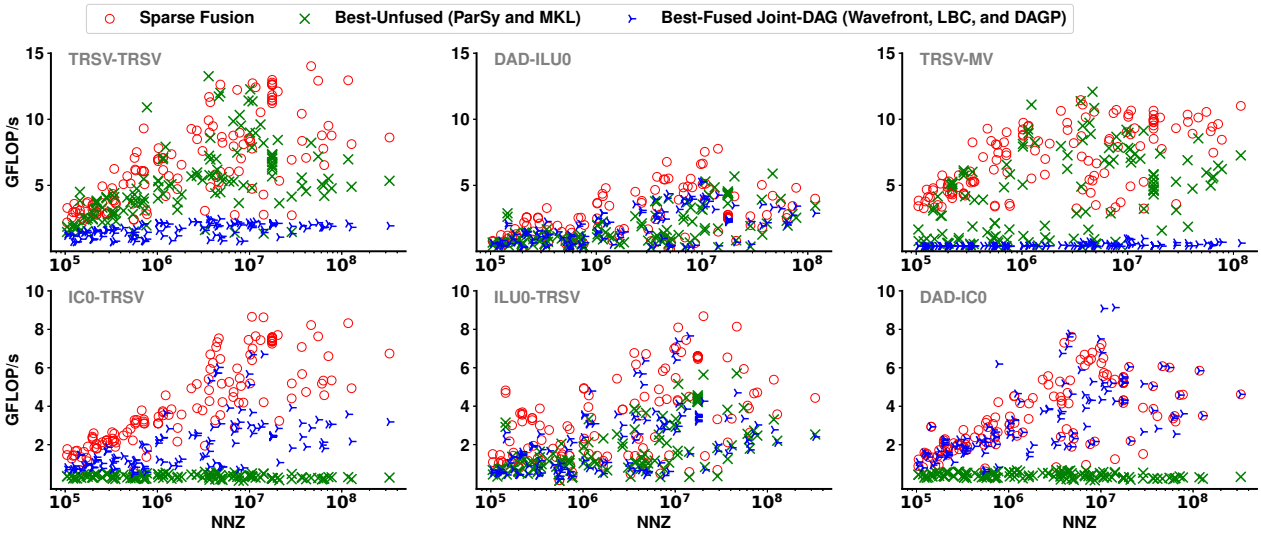

Figure 5: Performance of different implementations shown in GFLOPs per second.

carried dependencies, and a variety of memory access pattern behaviour. For example, combinations of SpTRSV, $Lx = b$ and SpMV are main bottlenecks in conjugate gradient methods [4, 52], GMRES [11], Gauss-Seidel [32]. Preconditioned Krylov methods [20] and Newton solvers [35] frequently use kernel combinations 3, 5, 6, 7. The s-step Krylov solvers [6] and s-step optimization methods used in machine learning [35] provide even more opportunities to interleave iterations. Thus, they use these kernel combinations significantly more than their classic formulations.

4.2 Sparse Fusion Performance.

Figure 5 shows the performance of the fused code from sparse fusion, the best-unfused implementation from ParSy and MKL, and the best-fused wavefront, fused LBC, and fused DAGP implementations. We report the minimum execution time of ParSy and MKL per matrix for each unfused data point in Figure 5. For each fused data point in Figure 5, we report the minimum execution time of fused wavefront, fused LBC, and fused DAGP per each matrix. The performance of implementations is shown in floating point operations per second (GFLOP/s). The theoretical floating point operations are computed per kernel combination and matrix and used for all implementations. Sparse fusion is on average 4.2× and 4× faster than the best unfused and fused implementations, respectively. For all kernel combinations and matrices shown in Figure 5, sparse fusion provides the fastest execution time in 76% of instances compared to the best fused and unfused implementations. Even though sparse fusion is on average 11.5× faster than MKL for ILU0-TRSV, since ILU0 only has a sequential implementation in MKL, the speedup of this kernel combination is excluded from the average speedups.

Locality in Sparse Fusion. The efficiency of the reuse ratio differs per kernel properties. Kernel combinations 1, 2, 4, 5, and 6 share the sparse matrix L and thus have a reuse ratio larger than one, while combination 3 only shares vector y,

leading to a reuse ratio lower than one. The selected packing strategy in sparse fusion improves the performance in 88% of kernel combinations and matrices and provides a 1-3.9× improvement in both categories. The highest improvement belongs to kernel combination 1, where accessing L values dominates the execution time, and reusing them after interleaved packing always leads to improvement. In kernel combinations including SpILU0 and SpIC0, the effect is lower since the accesses are more irregular than the rest.

Figure 6 top shows the average memory access latency [21] of sparse fusion, the fastest unfused implementation (ParSy), and the fastest fused partitioning-based implementation (Fused LBC) for all kernel combinations normalized over the ParSy average memory access latency (shown for matrix *bone010* as an example, other matrices exhibit similar behavior). The average memory access latency is used as a proxy for locality and is computed using the number of accesses to L1, LLC, and TLB measured with PAPI performance counters [42].

For kernels 1, 2, 4, 5, and 6 where the reuse ratio is larger than one, the memory access latency of ParSy is on average 1.3× larger than that of sparse fusion. Because of their high reuse ratio, these kernels benefit from optimizing locality between kernels made possible via interleaved packing. ParSy optimizes locality in each kernel individually. When applied to the joint DAG, LBC can potentially improve the temporal locality between kernels and thus there is only a small gap between the memory access latency of sparse fusion and that of fused LBC. For kernel combination 3 where the reuse ratio is smaller than one, the gap between the memory access latency of sparse fusion and fused LBC is larger than the gap between the memory access latency of sparse fusion and ParSy. Sparse fusion and ParSy both improve data locality within each kernel for these kernel combinations.

Load Balance and Synchronization in Sparse Fusion. Figure 6 bottom shows the OpenMP potential gain [34] of sparse fusion, ParSy, and Fused LBC for all kernel combinations normalized over ParSy's potential gain (shown for matrix *bone010* as an example). The OpenMP potential gain is a metric in Vtune [53] that shows the total parallelism overhead, e.g., wait-time due to load imbalance and synchronization overhead, divided by the number of threads. This metric is used to measure the load imbalance and synchronization overhead in ParSy, fused LBC, and sparse fusion.

Kernel combination 3 has slack vertices that provide opportunities to balance workloads. For example, for the studied matrices, between 39-82% of vertices can be slacked, thus the potential gain balance of ParSy is 1.6× larger than that of sparse fusion and 2.4× lower than that of fused LBC. ParSy can only improve load balance using the workloads of an individual kernel. As shown in Figure 1, for kernel combination 4, the joint DAG has a small number of parallel iterations

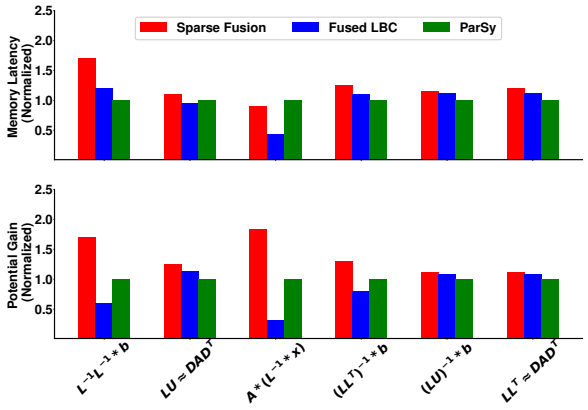

Figure 6: Average memory access latency (top) and the OpenMP potential gain (bottom) for matrix *bone010*. The legends show the implementation, values are normalized over ParSy.

in the final wavefronts that makes the final s-partitions of the LBC fused implementation imbalanced (a similar trend exists for kernel combination 5). For these kernel combinations, the code from sparse fusion has on average 33% fewer synchronization barriers compared to ParSy due to merging. For kernel combinations 1, 2, 3, and 6, the potential gain in sparse fusion is 1.3× less than that of ParSy. Merging in sparse fusion reduces the number of synchronizations in the fused code on average by 50% compared to that of ParSy. The sparsity pattern of matrices has a direct influence on thread parallelism. To ensure sufficient parallel iterations, all matrices are reordered with METIS, which also allows different schedulers to enhance the load balance. The exploration of techniques that do not rely on METIS is a topic for future work.

Inspector Time. Figure 7 shows the number of times that the executor should run to amortize the cost of inspection for implementations that have an inspector. For space reasons, only combinations 3 and 5 are shown, others follow the same trend. The number of executor runs (NER) that amortize the cost of inspector for an implementation is calculated using $\frac{Inspector\ Time}{Baseline\ Time - Executor\ Time}$. The *baseline* time is obtained by running each kernel individually with a sequential implementation, and the inspector and executor times belong to the specific implementation. When NER is negative, it means the inspector is not amortized in that tool. The fused LBC implementation has a NER of 3.1-745. The high inspection time is because of the high cost of converting the joint DAG into a chordal DAG, typically consuming 64% of its inspection time. The NER of the fused DAGP implementation is either negative or higher than 80. The fused wavefront implementation sometimes has a negative NER because the executor time

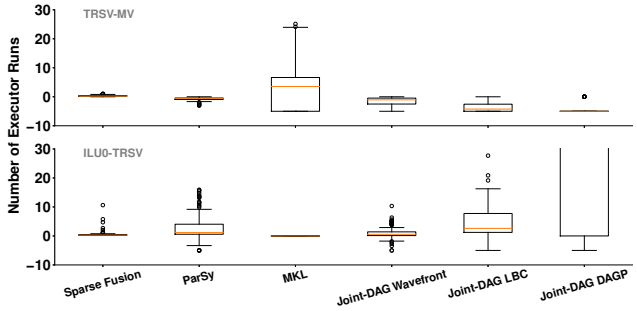

Figure 7: The number of executor runs to amortize inspector cost. Values are clipped between -10 and 30. (lower and positive values are better)

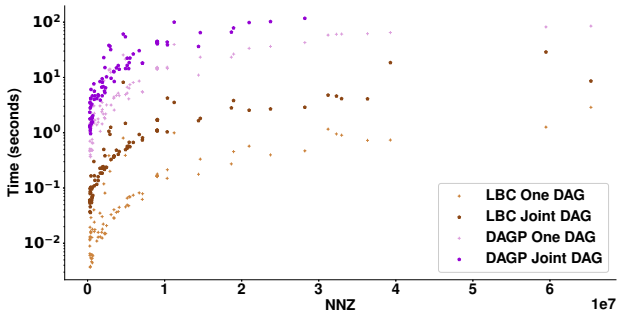

Figure 8: Performance of DAGP and LBC DAG partitioners for DAGs with different number of edges in an individual and joint DAG from fusing SpTRSV with SpMV kernels (lower is better)

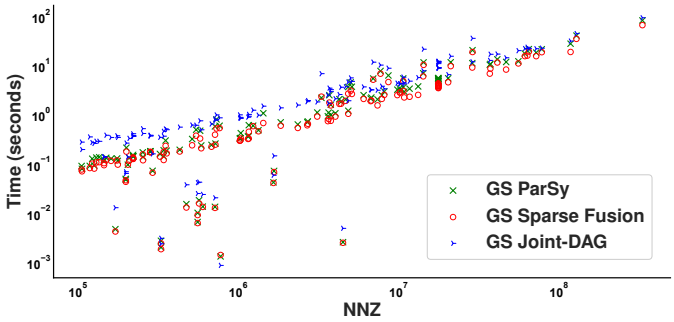

Figure 9: Performance of Guass-Seidel (GS) using unfused (GS ParSy) and fused implementations, i.e. sparse fusion (GS Sparse Fusion) and best of joint DAG methods (GS Joint-DAG) for matrices of different nonzeros. (lower is better)

is slower than the baseline time. As shown, sparse fusion, MKL, and ParSy have the lowest NER among all implementations. Sparse fusion's low inspection time is due to pairing strategies that enable partitioning one DAG at a time. Kernel combinations such as SpIC0-TRSV and SpILU0-TRSV only need one iteration to amortize the inspection time and SpTRSV-SpMV, SpTRSV-SpTRSV, and SpMV-SpTRSV need between 11-50 iterations. Sparse kernel combinations are routinely used in iterative solvers in scientific applications. Even with preconditioning, these solvers typically converge to an accurate solution after tens of thousands of iterations [4, 11, 27], hence amortizing the overhead of inspection.

Figure 8 compares the performance of two DAG partitioners, DAGP and LBC, for different sizes of sparse DAGs to demonstrate the expensive inspection time of fused joint-DAG implementations in Figure 7. In the one-DAG configuration, the DAG partitioner partitions the DAG of sparse triangular solve (SpTRSV) CSR. In the joint DAG configuration, the DAG partitioner partitions the joint DAG of the sparse matrix-vector multiplication (SpMV) CSR and SpTRSV CSR. To compare the joint DAG configuration with the one-DAG configuration, the x-axis shows the number of edges in one of the DAGs, i.e., SpTRSV DAG. The number of edges in the joint DAG is three times the number of edges in the SpTRSV DAG. As shown in Figure 8, DAGP in both one-DAG and joint-DAG configurations is slower than LBC for both small and large-size DAGs. Also, DAGP on the joint DAG runs out of memory for the last seven large DAGs (hence not shown in the figure).

4.3 Sparse Fusion Extension

We discuss the potential for sparse fusion when fusing more than two loops and parallel loops.

Gauss-Seidel, a case study for fusing more than two loops. To demonstrate the efficiency of sparse fusion in merging more than two loops, we use Gauss-Seidel (GS) [32] as an end-to-end case study. GS iteratively solves for the unknown vector x in $Ax = b$ where A is a sparse symmetric matrix stored in a CSR format, and b is a vector. We specifically use backward GS [32] that in its i^{th} iteration updates the solution by computing $(D - F)x_{i+1} = Ex_i + b$ where D, F, and E are diagonal, lower triangular, and upper triangular matrices with a decomposition of $A = D - F - E$, respectively. Each iteration of GS computes an SpMV followed by SpTRSV. By unrolling the outermost loop of GS, Sparse Fusion has the opportunity to fuse more than two loops, e.g., unrolling one iteration exposes four kernels/loops for fusion; unrolling loops of iterative solvers for performance is a commonly used approach, e.g., s-step solvers [6].

The choice of SPD matrices guarantees convergence in GS. The linear system corresponding to each matrix is solved for either the accuracy threshold of 10^{-6} or the most accurate solution after 1000 iterations. To detect profitable loops for sparse fusion and joint-DAG approaches, we exhaustively

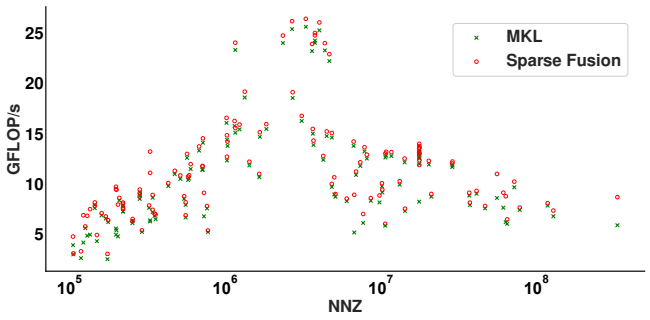

Figure 10: Performance of fused SpMV-SpMV in sparse fusion compared with the unfused MKL performance

search for a fusion of 2–6 loops and select the fastest code. Figure 9 compares the performance of GS using sparse fusion (GS Sparse Fusion), ParSy (GS ParSy), and the best of joint-DAG implementations (GS Joint-DAG) for all the selected matrices. In more than 96% of the matrices, GS-Sparse-Fusion is faster than GS ParSy and GS joint-DAG. GS Sparse Fusion also provides an average speedup of 1.3× and 1.8× over GS ParSy and GS Joint-DAG, respectively, demonstrating the efficiency of sparse fusion when fusing more than two loops to accelerate iterative solvers. We also found that fusing more than 6 loops does not lead to improvement. In the reported execution times for sparse fusion in Figure 9, 37%, 8%, and 55% of data points are obtained from fusing two, four, and six loops respectively. This indicates the value of fusing more than two loops in iterative solvers.

Fusing parallel loops. While sparse fusion and ICO are designed for loops with carried dependence, they can also be used to fuse parallel loops, such as the sparse matrix-vector product (SpMV) with SpMV. Figure 10 compares the performance of fused SpMV-SpMV with the unfused MKL implementation. As shown, sparse fusion provides an average speedup of 1.18× over MKL. The sparse fusion implementation does not benefit from vector instructions, while MKL is a highly-optimized code. Sparse fusion focuses on thread parallelism and improves zero-stride (temporal locality) and unit-stride (spatial locality), potentially improving vectorization when combined with existing vectorization techniques [8, 47] for sparse matrix kernels.

5 RELATED WORK

Parallel implementations of individual sparse matrix kernels exist in both highly-optimized libraries [22, 29] and compiler frameworks [2, 9, 31, 40, 48]. High-performance sparse libraries optimize a sparse kernel such as [43, 45, 49] optimizes SpTRSV, [3, 28] optimizes SpMV, and MKL [46] contains optimized versions of several sparse kernels individually. Compiler frameworks such as Sympiler [7, 9, 12] and sparse polyhedral framework [40] also provide techniques to optimize a sparse kernel with loop-carried dependence. These libraries and frameworks provide an efficient implementation for their supported sparse kernels.

Inspector-executor frameworks commonly use wavefront parallelism [19, 44] to parallelize sparse matrix computations with loop-carried dependencies. Recently, task coarsening approaches such as LBC [10], HDagg [50] and DAGP [23] coarsen wavefronts and thus generate code that is optimized for parallelism, load balance, and locality. While available approaches can provide efficient optimizations for sparse kernels with or without loop-carried dependencies, they can only optimize sparse kernels individually.

A number of libraries and compiler frameworks provide parallel implementations of fused sparse kernels with no loop-carried dependencies, such as tensor multiplication kernels in ReACT [51] and SparseLNR [17], two or more SpMV kernels [24, 30] or SpMV and dot products [1, 16, 18]. The formulation of *s*-step Krylov solvers [6] has enabled iterations of iterative solvers to be interleaved and hence multiple SpMV kernels are optimized simultaneously by replicating computations to minimize communication costs [24, 30]. Sparse tiling [37–39, 41] is an inspector executor approach that uses manually written inspectors [37, 39] to group iterations of different loops of a specific kernel such as Gauss-Seidel [39] and Moldyn [37] and is generalized for parallel loops without loop-carried dependencies [41]. Sparse fusion optimizes combinations of sparse kernels where at least one of the kernels has loop-carried dependencies.

6 CONCLUSION

We present sparse fusion and demonstrate how it improves parallelism, load balance, and data locality in sparse matrix combinations compared to when sparse kernels are optimized separately. Sparse fusion inspects the DAGs of the input sparse kernels and uses the ICO algorithm to balance the workload between wavefronts and determine whether to optimize data locality within or between the kernels. Sparse fusion's generated code outperforms state-of-the-art implementations for sparse matrix optimizations. In future work, we plan to investigate strategies that enable sparse fusion for arbitrary sparse operations.

ACKNOWLEDGMENTS

We thank the reviewers for their constructive feedback. This work is supported by NSERC Discovery Grants (RGPIN-06516, DGECR00303, RGPIN-2023-04897, DGECR-2023-00133), National Science Foundation (NSF CCF-2106621), the Canada Research Chairs program, the Ontario Early Researcher Award, Chameleon Project [26] and the Digital Research Alliance of Canada (www.alliancecan.ca).

REFERENCES

[1] Emmanuel Agullo, Jim Demmel, Jack Dongarra, Bilel Hadri, Jakub Kurzak, Julien Langou, Hatem Ltaief, Piotr Luszczek, and Stanimire Tomov. 2009. Numerical linear algebra on emerging architectures: The PLASMA and MAGMA projects. In *Journal of Physics: Conference Series*, Vol. 180. IOP Publishing, 012037.

[2] Willow Ahrens, Daniel Donenfeld, Fredrik Kjolstad, and Saman Amarasinghe. 2023. Looplets: A Language for Structured Coiteration. In *Proceedings of the 21st ACM/IEEE International Symposium on Code Generation and Optimization*. 41–54.

[3] Arash Ashari, Naser Sedaghati, John Eisenlohr, Srinivasan Parthasarath, and P Sadayappan. 2014. Fast sparse matrix-vector multiplication on GPUs for graph applications. In *SC'14: Proceedings of the International Conference for High Performance Computing, Networking, Storage and Analysis*. IEEE, 781–792.

[4] Michele Benzi, Jane K Cullum, and Miroslav Tuma. 2000. Robust approximate inverse preconditioning for the conjugate gradient method. *SIAM Journal on Scientific Computing* 22, 4 (2000), 1318–1332.

[5] Stephen Boyd, Stephen P Boyd, and Lieven Vandenberghe. 2004. *Convex optimization*. Cambridge university press.

[6] Erin Claire Carson. 2015. *Communication-avoiding Krylov subspace methods in theory and practice*. Ph. D. Dissertation. UC Berkeley.

[7] Kazem Cheshmi. 2022. *Transforming Sparse Matrix Computations*. Ph. D. Dissertation. University of Toronto (Canada).

[8] Kazem Cheshmi, Zachary Cetinic, and Maryam Mehri Dehnavi. 2022. Vectorizing sparse matrix computations with partially-strided codelets. In *SC22: International Conference for High Performance Computing, Networking, Storage and Analysis*. IEEE, 1–15.

[9] Kazem Cheshmi, Shoaib Kamil, Michelle Mills Strout, and Maryam Mehri Dehnavi. 2017. Sympiler: transforming sparse matrix codes by decoupling symbolic analysis. In *Proceedings of the International Conference for High Performance Computing, Networking, Storage and Analysis*. 1–13.

[10] Kazem Cheshmi, Shoaib Kamil, Michelle Mills Strout, and Maryam Mehri Dehnavi. 2018. ParSy: inspection and transformation of sparse matrix computations for parallelism. In *SC18: International Conference for High Performance Computing, Networking, Storage and Analysis*. IEEE, 779–793.

[11] Kazem Cheshmi, Danny M Kaufman, Shoaib Kamil, and Maryam Mehri Dehnavi. 2020. NASOQ: numerically accurate sparsity-oriented QP solver. *ACM Transactions on Graphics (TOG)* 39, 4 (2020), 96–1.

[12] Kazem Cheshmi, Michelle Mills Strout, and Maryam Mehri Dehnavi. 2022. Optimizing sparse computations jointly. In *Proceedings of the 27th ACM SIGPLAN Symposium on Principles and Practice of Parallel Programming*. 459–460.

[13] Edmond Chow and Aftab Patel. 2015. Fine-grained parallel incomplete LU factorization. *SIAM journal on Scientific Computing* 37, 2 (2015), C169–C193.

[14] Timothy A Davis. 2006. *Direct methods for sparse linear systems*. SIAM.

[15] Timothy A Davis and Yifan Hu. 2011. The University of Florida sparse matrix collection. *ACM Transactions on Mathematical Software (TOMS)* 38, 1 (2011), 1.

[16] Maryam Mehri Dehnavi, David M Fernández, and Dennis Giannacopoulos. 2011. Enhancing the performance of conjugate gradient solvers on graphic processing units. *IEEE Transactions on Magnetics* 47, 5 (2011), 1162–1165.

[17] Adhitha Dias, Kirshanthan Sundararajah, Charitha Saumya, and Milind Kulkarni. 2022. SparseLNR: accelerating sparse tensor computations using loop nest restructuring. In *Proceedings of the 36th ACM International Conference on Supercomputing*. 1–14.

[18] Pieter Ghysels and Wim Vanroose. 2014. Hiding global synchronization latency in the preconditioned conjugate gradient algorithm. *Parallel Comput.* 40, 7 (2014), 224–238.

[19] R Govindarajan and Jayvant Anantpur. 2013. Runtime dependence computation and execution of loops on heterogeneous systems. In *Proceedings of the 2013 IEEE/ACM International Symposium on Code Generation and Optimization (CGO)*. IEEE Computer Society, 1–10.

[20] Laura Grigori and Sophie Moufawad. 2015. Communication avoiding ILU0 preconditioner. *SIAM Journal on Scientific Computing* 37, 2 (2015), C217–C246.

[21] John L Hennessy and David A Patterson. 2017. *Computer architecture: a quantitative approach*. Elsevier.

[22] Pascal Hénon, Pierre Ramet, and Jean Roman. 2002. PASTIX: a high-performance parallel direct solver for sparse symmetric positive definite systems. *Parallel Comput.* 28, 2 (2002), 301–321.

[23] Julien Herrmann, M Yusuf Ozkaya, Bora Uçar, Kamer Kaya, and Ümit VV Çatalyürek. 2019. Multilevel algorithms for acyclic partitioning of directed acyclic graphs. *SIAM Journal on Scientific Computing* 41, 4 (2019), A2117–A2145.

[24] Mark Hoemmen. 2010. *Communication-avoiding Krylov subspace methods*. University of California, Berkeley.

[25] George Karypis and Vipin Kumar. 1998. A software package for partitioning unstructured graphs, partitioning meshes, and computing fill-reducing orderings of sparse matrices. *University of Minnesota, Department of Computer Science and Engineering, Army HPC Research Center, Minneapolis, MN* (1998).

[26] Kate Keahey, Jason Anderson, Zhuo Zhen, Pierre Riteau, Paul Ruth, Dan Stanzione, Mert Cevik, Jacob Colleran, Haryadi S. Gunawi, Cody Hammock, Joe Mambretti, Alexander Barnes, François Halbach, Alex Rocha, and Joe Stubbs. 2020. Lessons Learned from the Chameleon Testbed. In *Proceedings of the 2020 USENIX Annual Technical Conference (USENIX ATC '20)*. USENIX Association.

[27] David S Kershaw. 1978. The incomplete Cholesky-conjugate gradient method for the iterative solution of systems of linear equations. *Journal of computational physics* 26, 1 (1978), 43–65.

[28] Jiajia Li, Guangming Tan, Mingyu Chen, and Ninghui Sun. 2013. SMAT: an input adaptive auto-tuner for sparse matrix-vector multiplication. In *Proceedings of the 34th ACM SIGPLAN conference on Programming language design and implementation*. 117–126.

[29] Xiaoye S Li. 2005. An overview of SuperLU: Algorithms, implementation, and user interface. *ACM Transactions on Mathematical Software (TOMS)* 31, 3 (2005), 302–325.

[30] M. MehriDehnavi, Y. El-Kurdi, J. Demmel, and D. Giannacopoulos. 2013. Communication-Avoiding Krylov Techniques on Graphic Processing Units. *IEEE Transactions on Magnetics* 49, 5 (2013), 1749–1752. https://doi.org/10.1109/TMAG.2013.2244861

[31] Mahdi Soltan Mohammadi, Tomofumi Yuki, Kazem Cheshmi, Eddie C Davis, Mary Hall, Maryam Mehri Dehnavi, Payal Nandy, Catherine Olschanowsky, Anand Venkat, and Michelle Mills Strout. 2019. Sparse computation data dependence simplification for efficient compiler-generated inspectors. In *Proceedings of the 40th ACM SIGPLAN Conference on Programming Language Design and Implementation*. 594–609.

[32] Yousef Saad. 2003. *Iterative methods for sparse linear systems*. SIAM.

[33] Yousef Saad and Andrei V Malevsky. 1995. P-Sparslib: a portable library of distributed memory sparse iterative solvers. In *Proceedings of Parallel Computing Technologies (PaCT-95), 3-rd international conference, St. Petersburg*. Citeseer.

[34] Intel Software. 2018. *OpenMP potential gain definition in intel VTune*. https://software.intel.com/content/www/us/en/develop/documentation/vtune-help/top/reference/cpu-metrics-reference/openmp-potential-gain.html

[35] Saeed Soori, Aditya Devarakonda, Zachary Blanco, James Demmel, Mert Gurbuzbalaban, and Maryam Mehri Dehnavi. 2018. Reducing communication in proximal Newton methods for sparse least squares problems. In *Proceedings of the 47th International Conference on Parallel Processing*. 1–10.

[36] Bartolomeo Stellato, Goran Banjac, Paul Goulart, Alberto Bemporad, and Stephen Boyd. 2020. OSQP: An operator splitting solver for quadratic programs. *Mathematical Programming Computation* (2020), 1–36.

[37] Michelle Mills Strout, Larry Carter, and Jeanne Ferrante. 2003. Compile-time composition of run-time data and iteration reorderings. In *Proceedings of the ACM SIGPLAN 2003 conference on Programming language design and implementation*. 91–102.

[38] Michelle Mills Strout, Larry Carter, Jeanne Ferrante, Jonathan Freeman, and Barbara Kreaseck. 2002. Combining performance aspects of irregular gauss-seidel via sparse tiling. In *International Workshop on Languages and Compilers for Parallel Computing*. Springer, 90–110.

[39] Michelle Mills Strout, Larry Carter, Jeanne Ferrante, and Barbara Kreaseck. 2004. Sparse tiling for stationary iterative methods. *The International Journal of High Performance Computing Applications* 18, 1 (2004), 95–113.

[40] Michelle Mills Strout, Mary Hall, and Catherine Olschanowsky. 2018. The sparse polyhedral framework: Composing compiler-generated inspector-executor code. *Proc. IEEE* 106, 11 (2018), 1921–1934.

[41] Michelle Mills Strout, Fabio Luporini, Christopher D Krieger, Carlo Bertolli, Gheorghe-Teodor Bercea, Catherine Olschanowsky, J Ramanujam, and Paul HJ Kelly. 2014. Generalizing run-time tiling with the loop chain abstraction. In *2014 IEEE 28th International Parallel and Distributed Processing Symposium*. IEEE, 1136–1145.

[42] Dan Terpstra, Heike Jagode, Haihang You, and Jack Dongarra. 2010. Collecting performance data with PAPI-C. In *Tools for High Performance Computing 2009*. Springer, 157–173.

[43] Ehsan Totoni, Michael T Heath, and Laxmikant V Kale. 2014. Structure-adaptive parallel solution of sparse triangular linear systems. *Parallel Comput.* 40, 9 (2014), 454–470.

[44] Anand Venkat, Mahdi Soltan Mohammadi, Jongsoo Park, Hongbo Rong, Rajkishore Barik, Michelle Mills Strout, and Mary Hall. 2016. Automating wavefront parallelization for sparse matrix computations. In *Proceedings of the International Conference for High Performance Computing, Networking, Storage and Analysis*. IEEE Press, 41.

[45] Richard Vuduc, Shoaib Kamil, Jen Hsu, Rajesh Nishtala, James W Demmel, and Katherine A Yelick. 2002. Automatic performance tuning and analysis of sparse triangular solve. ICS.

[46] Endong Wang, Qing Zhang, Bo Shen, Guangyong Zhang, Xiaowei Lu, Qing Wu, and Yajuan Wang. 2014. Intel math kernel library. In *High-Performance Computing on the Intel® Xeon Phi™*. Springer, 167–188.

[47] Lucas Wilkinson, Kazem Cheshmi, and Maryam Mehri Dehnavi. 2023. Register Tiling for Unstructured Sparsity in Neural Network Inference. *Proceedings of the ACM on Programming Languages* 7, PLDI (2023), 1995–2020.

[48] Zihao Ye, Ruihang Lai, Junru Shao, Tianqi Chen, and Luis Ceze. 2023. SparseTIR: Composable abstractions for sparse compilation in deep learning. In *Proceedings of the 28th ACM International Conference on Architectural Support for Programming Languages and Operating Systems, Volume 3*. 660–678.

[49] Buse Yılmaz, Buğrra Sipahioğrlu, Najeeb Ahmad, and Didem Unat. 2020. Adaptive Level Binning: A New Algorithm for Solving Sparse Triangular Systems. In *Proceedings of the International Conference on High Performance Computing in Asia-Pacific Region*. 188–198.

[50] Behrooz Zarebavani, Kazem Cheshmi, Bangtian Liu, Michelle Mills Strout, and Maryam Mehri Dehnavi. 2022. HDagg: hybrid aggregation of loop-carried dependence iterations in sparse matrix computations. In *2022 IEEE International Parallel and Distributed Processing Symposium (IPDPS)*. IEEE, 1217–1227.

[51] Tong Zhou, Ruiqin Tian, Rizwan A Ashraf, Roberto Gioiosa, Gokcen Kestor, and Vivek Sarkar. 2022. ReACT: Redundancy-Aware Code Generation for Tensor Expressions. (2022).

[52] Sicong Zhuang and Marc Casas. 2017. Iteration-fusing conjugate gradient. In *Proceedings of the International Conference on Supercomputing*. 1–10.

[53] Intel Developer Zone. [n. d.]. Intel VTune Amplifier, 2017. *Documentation at the URL: https://software.intel.com/en-us/intel-vtune-amplifier-xe-support/documentation* ([n. d.]).